Characterizing heterogeneous properties of cerebral aneurysms with unknown stress-free geometry – a precursor to in vivo identification

Xuefeng Zhao[1]*, Madhavan L. Raghavan[2], Jia Lu[1]†

[1] *Department of Mechanical and Industrial Engineering, Center for Computer Aided Design*
The University of Iowa, Iowa City, IA 52242-1527, USA

[2] *Department of Biomedical Engineering*
The University of Iowa, Iowa City, IA 52242, USA

Abstract

Knowledge of elastic properties of cerebral aneurysm is crucial for understanding the biomechanical behavior of the lesion. However, characterizing tissue properties using *in vivo* motion data presents a tremendous challenge. Aside from the limitation of data accuracy, a pressing issue is that the *in vivo* motion does not expose the stress-free geometry. This is compounded by the nonlinearity, anisotropy, and heterogeneity of the tissue behavior. This article introduces a method for identifying the heterogeneous properties of aneurysm wall tissue under unknown stress-free configuration. In the proposed approach, an accessible configuration is taken as the reference; the unknown stress-free configuration is represented locally by a metric tensor describing the pre-strain from the stress-free configuration to the reference configuration. Material parameters are identified together with the metric tensor point-wisely.

*Presently at: Department of Biomedical Engineering, Indiana University Purdue University Indianapolis, Indianapolis, IN 46202, USA.

†Corresponding author. Email address: jia-lu@uiowa.edu. Tel: +1-319 3356405. Fax: +1-319 3545669.

The paradigm is tested numerically using a forward-inverse analysis loop. An image-derived sac is considered. The aneurysm tissue is modeled as an eight-ply laminate whose constitutive behavior is described by an anisotropic hyperelastic strain-energy function containing four material parameters. The parameters are assumed to vary continuously in two assigned patterns to represent two types of material heterogeneity. Nine configurations between the diastolic and systolic pressures are generated by forward quasi-static finite element analyses. These configurations are fed to the inverse analysis to delineate the material parameters and the metric tensor. The recovered and the assigned distributions are in good agreement. A forward verification is conducted by comparing the displacement solutions obtained from the recovered and the assigned material parameters at a different pressure. The nodal displacements are found in excellent agreement.

Keywords: Cerebral aneurysms; tissue property; pointwise identification method; in vivo identification

1 Introduction

Cerebral aneurysms (CAs) are thin-walled dilatations of the intracranial arterial wall that usually develop in or near the circle of Willis. They may remain stable or may suddenly rupture. Rupture of CAs is the leading cause of subarachnoid hemorrhage [1]. At present, rupture risk assessment is based primarily on size and shape [2, 3, 4, 5, 6, 7, 8, 9], although mechanical factors such as stress and strain have also been submitted as indicators [10, 11, 12, 13]. It has been suggested that changes in the wall properties can contribute to the assessment of pathological development [14, 15] and thus, the tissue property could be an important biomarker. Needless to

say, knowledge of tissue properties is fundamental for biomechanical analysis.

Characterizing CA tissues *in vivo* faces some tremendous challenges. Due to the requirement of non-invasiveness and the lack of control over the deformation and load, the characterization must rely on the wall motion and blood pressure data obtained from diagnosis. Unfortunately, it is generally agreed that current diagnostic tools are unable to accurately resolve the wall motion. A recent study by Balocco et al. concluded that the spatial resolution of medical images is insufficient to support *in vivo* tissue property identification using a reverse finite element optimization method [16]. Even if imaging technology would eventually provide sufficiently accurate motion data, as is expected to happen in future, there are other obstacles that can hamper the analysis. First, the visible pulsation, which corresponds to the motion between the diastolic and the systolic pressures, does not expose the stress-free geometry of the lesion. This is a fundamental issue facing the inverse characterization of vascular tissues. Secondly, aneurysm tissues are generally nonlinear, anisotropic, and heterogeneous. Describing the property distribution requires a large number of parameters. The traditional inverse approach which simultaneously estimates all parameters can easily lead to lack of robustness related to the presence of local minima and prohibitively expensive computations.

The pointwise identification method (PWIM) [17, 18] developed recently by the present authors offers an alternative for characterizing heterogeneous thin materials. The method exploits the property of static determinacy of curved (deep) membrane structures to compute the wall stress without invoking the material properties in question. Stress distributions are computed using the inverse elastostatic method [19, 20, 21, 22, 13], which directly takes a deformed state as input. The method utilizes an auxiliary material model, but the resulting stress is expected to depend minimally on the model. Compared to traditional approaches, a distinct feature of PWIM is that it

circumvents global optimization problems. The optimization problem is formulated at each material point using pointwise stress-strain data, and solved individually. In this way, the optimization problem is not tied to the meshsize, but only the constitutive law. The method was tested on a cerebral aneurysm model and was found effective in characterizing complicated nonlinear anisotropic materials [23]. However, in [23] the stress-free configuration was assumed to be known, mimicking a typical *in vitro* setting.

The purpose of this paper is to advance PWIM to consider unknown stress-free configuration and test the feasibility of simultaneously identifying material parameters and geometry. This study is an indispensable step towards *in vivo* application. Although *in vivo* identification is currently impractical due to the limitation of image resolution, preparatory studies like this help to resolve other technical issues and to understand the potential of *in vivo* identification. The fact that the vascular stress-free configuration is unknown *in vivo* presents no real challenge to stress analysis. Stress analysis can be conducted using the inverse elastostatic method [19, 20] which formulates the equilibrium problem directly on a deformed configuration. Recently, some research groups, including the authors', have applied the concept to vascular problems [21, 13, 22, 24, 25, 26, 27]. For cerebral aneurysms and thin-walled saccular structures alike, the inverse method has an additional advantage that it can sharply capitalize on the static determinacy of the system and enables stress analysis without using the realistic material constitutive equation [13, 25]. This is significant for patient-specific studies because truly patient-specific material parameters are rarely available. In contrast, the lack of knowledge of the stress-free configuration is a serious issue for tissue characterization, as the strain is unknown without a reference. Characterizing tissue properties without knowing the stress-free configuration requires a simultaneous estimation of elastic parameters and geometry. To the best

knowledge of the authors, there are no successful case studies of this type reported in the literature.

In [17], the authors proposed the idea of presenting unknown stress-free geometry by local parameters and identifying them simultaneously with the material constants within the pointwise framework. The unknown stress-free geometry is treated locally as an initial strain, and represented by a metric tensor referred to as the reference metric. The premise is that the reference metric, which plays a different role than elasticity constants in a constitutive description, can be distinguished from elasticity constants and identified simultaneously with the latter if the acquired stress-stain data sufficiently expose the constitutive behavior. Theoretical underpinnings of the metric-based constitutive formulation for pre-strained hyperelastic solids were discussed in [28]. For a membrane structure, the reference metric is a 2D tensor having three components. Hence, within the framework of PWIM, considering the unknown geometry amounts to adding three more parameters in the local optimization problem, which should not significantly increase the level of numerical difficulty. In this paper, we evaluate this approach numerically using a forward-inverse loop on an image-based aneurysm. To emulate *in vivo* conditions, only the motion data between the diastolic and the systolic pressures are made available to the inverse analysis. The aneurysm tissue is described by a nonlinear anisotropic constitutive equation with spatially varying elastic properties and symmetry axes.

The remainder of this paper is organized as follows. Section 2 discusses the kinematic description used in this study, with a particular emphasis on the representation of stress-free configuration. This representation is later utilized in the tissue constitutive model to establish stress functions containing unknown initial strains. Section 3 documents the numerical study, providing a detailed description of the material model, computation procedure, and algorithmic settings. Section 4 presents numer-

ical results. Discussions on the methodology and results are contained in Section 5.

2 Membrane kinematics

We utilize the standard convected coordinate description to formulate the kinematics of a curved membrane. The membrane surface is parameterized by curvilinear coordinates (ξ^1, ξ^2) for which a pair of coordinates $P = (\xi^1, \xi^2)$ represents a material point throughout the motion. Since the stress-free configuration is in general not known, we take an accessible configuration $\mathscr{C} \in \mathbb{R}^3$ as the reference, and denote the position of a material point by $\mathbf{X} = \mathbf{X}(P)$. The position of the same material point in the current configuration is denoted by $\mathbf{x} = \mathbf{x}(P)$. The surface coordinates induce a set of convected basis vectors $\mathbf{g}_\alpha = \frac{\partial \mathbf{x}}{\partial \xi^\alpha}$ $(\alpha = 1, 2)$ that propagate through all configurations, starting from the reference one where the bases are denoted as $\mathbf{G}_\alpha = \frac{\partial \mathbf{X}}{\partial \xi^\alpha}$. The surface deformation gradient, understood as a linear mapping between tangent spaces in the reference and the current configurations at a material point, is

$$\mathbf{F} = \mathbf{g}_\alpha \otimes \mathbf{G}^\alpha. \tag{1}$$

Here $\mathbf{G}^\alpha$ are the reciprocal (contravariant) bases, $\mathbf{G}^\alpha \cdot \mathbf{G}_\beta = \delta^\alpha_\beta$, $\mathbf{G}^\alpha \cdot \mathbf{A} = 0$ where $\mathbf{A}$ is the surface normal at $\mathbf{X}(P)$. The summation convention applies to repeated indices. The Cauchy-Green deformation tensor follows as

$$\mathbf{C} = \mathbf{F}^T\mathbf{F} = g_{\alpha\beta}\mathbf{G}^\alpha \otimes \mathbf{G}^\beta, \quad g_{\alpha\beta} = \mathbf{g}_\alpha \cdot \mathbf{g}_\beta. \tag{2}$$

From a geometric perspective, $\mathbf{C}$ can be regarded as a metric tensor (the pullback of the Euclidean metric) that describes the *current* geometry of the membrane. In fact, the fundamental form

$$ds^2 = d\mathbf{X} \cdot \mathbf{C} d\mathbf{X} \tag{3}$$

gives the current length of the line element $d\mathbf{X}$ in $\mathscr{C}$. Since the reference configuration is pre-strained, the Euclidean metric does not describe the natural (i.e., stress-free) geometry. We assume that there is a reference metric tensor $\mathfrak{G}$ at every point in $\mathscr{C}$ that defines the natural geometry. Having this metric tensor, the undistorted length of a line element $d\mathbf{X}$ is given by

$$dS_0^2 = d\mathbf{X} \cdot \mathfrak{G} d\mathbf{X}. \tag{4}$$

By assumption, the tensor $\mathfrak{G}$ is positive definite. It admits the following component form in the surface coordinate system:

$$\mathfrak{G} = \mathfrak{G}_{\alpha\beta} \mathbf{G}^\alpha \otimes \mathbf{G}^\beta. \tag{5}$$

Note that both $\mathbf{C}$ and $\mathfrak{G}$ are tensors in the reference configuration. They define bilinear forms that take two tangent vectors in $\mathscr{C}$ to generate a scalar. Although not necessary for the ensuing development, the metric $\mathfrak{G}$ is assumed to vary smoothly over the domain.

The following thought-experiment may shed light on the nature of $\mathfrak{G}$. If an infinitesimally small material element is cut out from the membrane and the external load releases, the element will relax to a stress-free state which we refer to as a local stress-free configuration. Let $\mathbf{K}^{-1}$ be the linear mapping that maps the infinitesimal element from its reference state in $\mathscr{C}$ to its local stress-free configuration. $\mathbf{K}^{-1}$ is determined if mappings on two linearly independent tangent vectors are known. If $(\boldsymbol{\mathcal{G}}_1 d\xi^1, \boldsymbol{\mathcal{G}}_2 d\xi^2)$ are images of line elements $(\mathbf{G}_1 d\xi^1, \mathbf{G}_2 d\xi^2)$, respectively, then

$$\mathbf{K}^{-1} = \boldsymbol{\mathcal{G}}_\alpha \otimes \mathbf{G}^\alpha. \tag{6}$$

The relaxed line element is $\mathbf{K}^{-1} d\mathbf{X} = \boldsymbol{\mathcal{G}}_1 d\xi^1 + \boldsymbol{\mathcal{G}}_2 d\xi^2$. Its length is given by

$$dS_0^2 = \left(\mathbf{K}^{-1} d\mathbf{X}\right) \cdot \left(\mathbf{K}^{-1} d\mathbf{X}\right) = d\mathbf{X} \cdot \left(\mathbf{K}^{-T} \mathbf{K}^{-1}\right) d\mathbf{X}. \tag{7}$$

Motivated by this computation, we can make the connection that

$$\mathfrak{G} = \mathbf{K}^{-T}\mathbf{K}^{-1}, \quad \mathfrak{G}_{\alpha\beta} = \boldsymbol{\mathcal{G}}_\alpha \cdot \boldsymbol{\mathcal{G}}_\beta. \tag{8}$$

Remarks

1. The concept of local stress-free configuration appears to be first proposed by Noll [29], who noted that *configurations* should be understood in a local sense, as the stress at a point depends only on the local motion in the vicinity of the point. In this sense, it is meaningful to identify a zero-stress configuration for each infinitesimal element individually. Here, $\mathbf{K}^{-1}$ defines a local stress-free configuration. During a regular motion, the stress should depend on $\mathbf{FK}$ where $\mathbf{F}$ is the deformation gradient relative to the chosen reference configuration. In this way, the natural geometry enters the constitutive description through the local mapping $\mathbf{K}$. This framework has been adapted in various constitutive theories, for example finite plasticity [30, 31], tissue growth [32, 33], residual stress [34, 35], and initial strains [36, 37, 38]. Stålhand et al. [36, 37, 38] used this description to formulate aorta inverse problems. However, as a general framework for parameter identification, this approach has a limitation related to the rotational indeterminacy of the local stress-free configuration. If $\mathbf{K}^{-1}$ brings a material element to a local stress-free configuration, so does $\mathbf{QK}^{-1}$ for a rotation tensor $\mathbf{Q}$ because a superposed rotation does not change the zero stress. If $\mathbf{K}^{-1}$ is to be determined inversely, the rotational indeterminacy will render the problem ill-posed. In contrast, the rotational indeterminacy is completely eliminated in the metric-based description.

2. If the membrane has a global stress-free configuration $\mathscr{C}_0$ in which positions of

material points are given by $\mathbf{X}_0(P)$, $\mathfrak{G}$ takes the form

$$\mathfrak{G}_{\alpha\beta} = \frac{\partial \mathbf{X}_0}{\partial \xi^\alpha} \cdot \frac{\partial \mathbf{X}_0}{\partial \xi^\beta}. \tag{9}$$

In this case, $\mathfrak{G}$ is derived from a global motion and is said to be compatible. In general, we do not require $\mathfrak{G}$ to be compatible. An implication of this assumption is that the structure may not have a global stress-free configuration. This feature is in fact desirable for vascular analysis as vascular organs are in general residually stressed.

Returning to kinematics, the change of geometry from the local stress-free configuration to the deformed state is completely determined by the pair of metric tensors $\mathbf{C}$ and $\mathfrak{G}$. In particular, the stretch of a line element $d\mathbf{X} = \mathbf{N}dS$ in $\mathscr{C}$ is given by

$$\lambda^2 = \frac{N^\alpha g_{\alpha\beta} N^\beta}{N^\delta \mathfrak{G}_{\delta\gamma} N^\gamma}. \tag{10}$$

Here N^α is the components of $\mathbf{N}$ in the convected basis system, $\mathbf{N} = N^\alpha \mathbf{G}_\alpha$. The invariant I_1, traditionally defined as $\mathrm{tr}\,(\mathbf{C})$ where $\mathbf{C}$ is the Cauchy-Green deformation tensor relative to the stress-free configuration, becomes

$$I_1 = \mathrm{tr}\,(\mathbf{C}\mathfrak{G}^{-1}). \tag{11}$$

If we introduce the contravariant components $\mathfrak{G}^{\alpha\beta}$ of $\mathfrak{G}$, defined by $\mathfrak{G}^{\alpha\beta}\mathfrak{G}_{\beta\gamma} = \delta^\alpha_\gamma$, then

$$I_1 = g_{\alpha\beta}\mathfrak{G}^{\alpha\beta}. \tag{12}$$

This invariant characterizes the average square stretch of all line elements emanating from a point. The invariant I_2, defined as the square area stretch for a material element, takes the form

$$I_2 = \det(\mathbf{C}\mathfrak{G}^{-1}) = \frac{\det[g_{\alpha\beta}]}{\det[\mathfrak{G}_{\delta\gamma}]}. \tag{13}$$

Any constitutive equations represented as functions of I_1, I_2, and line stretches can be readily expressed as functions of $\mathbf{C}$, $\mathfrak{G}$, and fiber direction $\mathbf{N}$. More details of this constitutive setting can be found in [28].

3 Numerical experiments

3.1 Material model

We utilized the aneurysmal tissue model proposed by Kroon and Holzapfel [39] to describe the constitutive behavior. The model was employed by the same authors recently in an inverse analysis of cerebral aneurysms [40]. Cerebral aneurysm wall consists of primarily 7-8 layers of type I and III collagen fibers with varying orientations that form two-dimensional networks [41]. At the continuum level, the tissue is described by a single strain energy function that takes into account collectively the property and microstructure of its constituents. In particular to Kroon-Holzapfel model, the energy function assumes the form

$$w = \sum_{I=1}^{8} \frac{k_I}{8a} \left(\exp[a(\lambda_I^2 - 1)^2] - 1 \right), \tag{14}$$

where, λ_I is the fiber stretch of the I-th fiber, k_I defines the fiber stiffness, and a is a dimensionless parameter. The energy function does not contain the usual isotropic term, reflecting the fact that aneurysmal tissues are depleted of elastin content. It is important to note that the energy function (14) is defined with respect to the natural state. The stretches λ_I are those measured from the local stress-free configuration. The energy function (14) is a surface density (strain energy per unit undeformed surface area); it is related to an underlying 3D energy function W via $w = HW$ where H is the undeformed wall thickness. Variables k_1 through k_8 are *effective* stiffness parameters, which are the product of 3D elasticity constants with the wall

thickness having the dimension of force per unit length. The stress function derived from this energy function is introduced later in Section 3.5.

In the current study, the angular distribution of fibers in the stress-free state was assumed to be uniform at every material point. Fiber angles ϕ_I with respect to the principal fiber directions were assigned according to

$$\phi_I = \frac{I-1}{8}\pi, \quad I = 1, 2, ..., 8. \tag{15}$$

The principal fiber directions, i.e., $\boldsymbol{\eta}_1$ and $\boldsymbol{\eta}_2$ in Figure 1, are aligned with the first and fifth fibers, respectively. These two directions define local orthotropic material axes. In the convected basis system $\{\boldsymbol{\mathcal{G}}_1, \boldsymbol{\mathcal{G}}_2\}$, the material axes are uniquely parameterized by the angle θ that $\boldsymbol{\eta}_1$ makes relative to $\boldsymbol{\mathcal{G}}_1$, see Figure 1.

It was further assumed that the fiber stiffness parameters k_I are symmetrically distributed with respect to the material axes. If we let k_1 be the fiber stiffness in the first principal direction and k_5 be the second (transverse) stiffness, the others take the value

$$\begin{aligned} k_I &= \frac{5-I}{4}k_1 + \frac{I-1}{4}k_5, \quad I = 2, 3, 4; \\ k_I &= \frac{9-I}{4}k_5 + \frac{I-5}{4}k_1, \quad I = 6, 7, 8. \end{aligned} \tag{16}$$

At the ground state (i.e., no distortion), the stiffness parameters in the material axes work out to be

$$E_1 := D_{1111} = \sum_{I=1}^{8} k_I \cos^4 \phi_I, \qquad E_2 := D_{2222} = \sum_{I=1}^{8} k_I \sin^4 \phi_I, \tag{17}$$

where $\phi_I = \{0, \frac{\pi}{8}, \frac{2\pi}{8}, \cdots, \frac{7\pi}{8}\}$. Equations (17) and (16) give a linear relation between (E_1, E_2) and (k_1, k_5):

$$\begin{bmatrix} E_1 \\ E_2 \end{bmatrix} = \begin{bmatrix} \frac{1}{4}(8+\sqrt{2}) & \frac{1}{4}(4-\sqrt{2}) \\ \frac{1}{4}(4-\sqrt{2}) & \frac{1}{4}(8+\sqrt{2}) \end{bmatrix} \begin{bmatrix} k_1 \\ k_5 \end{bmatrix}. \tag{18}$$

Hence, once E_1 and E_2 are given, the stiffness parameter for each fiber family is completely determined.

3.2 Generation of deformation data

Finite element simulations were conducted on an image based aneurysm sac to generate a series of deformed configurations. The wall tissue was modeled by Kroon-Holzapfel model introduced above. We studied two cases of property distribution. In Case I, the stiffness parameters were assumed to decrease linearly with respect to the height from the neck, viz.

$$E_i = E_i^{fundus} + \frac{E_i^{neck} - E_i^{fundus}}{Z^{neck} - Z^{fundus}}(Z - Z^{fundus}), \quad i = 1, 2. \tag{19}$$

Here Z is the "Z" coordinate of any point on the sac, Z^{fundus} and Z^{neck} are the "Z" coordinates at the fundus and neck, respectively. Similarly, E_i^{fundus} and E_i^{neck} are respectively the elasticity parameters at the fundus and neck; they were set to

$$\begin{aligned} E_1^{fundus} &= 0.45 \text{ N/mm}, \quad E_1^{neck} = 1.15 \text{ N/mm}, \\ E_2^{fundus} &= 0.35 \text{ N/mm}, \quad E_2^{neck} = 0.85 \text{ N/mm}. \end{aligned} \tag{20}$$

In Case II, the stiffness parameters were uniform in the dome region, $E_1^{fundus} = 0.8$ N/mm and $E_2^{fundus} = 0.6$ N/mm, with a smooth linear transition to those at the neck ($E_1^{neck} = 1.16$ N/mm and $E_2^{neck} = 0.88$ N/mm) according to Equation (19). This distribution was motivated by inflammatory conditions. Before rupture, inflammatory cell infiltration and smooth muscle cell proliferation increase in CA walls [42]. Proteases derived from inflammatory cells associated with atherosclerosis may compromise the structural integrity of the aneurysm and degrade the tissue stiffness [43]. The parameter a=20 was assumed to be uniformly distributed over the entire aneurysm sac. The reference distributions of the elastic parameters, E_1 and E_2, for Case I and Case II are shown in Figure 2.

In both cases, the principal symmetry axis $\boldsymbol{\eta}_1$ was assumed to be parallel to the basal (x-y) plane and tangent to the aneurysm surface at every point. The other

axis, $\boldsymbol{\eta}_2$, was point-wisely perpendicular to the first one (see Figure 3). The angle θ therefore varied from point to point.

For each case, a total of 9 loaded configurations were obtained in the pressure range of 80 to 160 mmHg at an interval of 10 mmHg. The imaged geometry was assumed to be the stress-free configuration; this configuration was later blinded to the stress analysis and inverse identification. The simulation was conducted using the forward nonlinear membrane finite element in FEAP, a nonlinear finite element program [44]. The finite element mesh consisted of 885 quadrilateral membrane elements and 916 nodes. Clamped boundary condition was applied at the neck of the aneurysm. This is not the realistic boundary condition *in vivo*, but was used for demonstrative purpose.

3.3 Strain acquisition

To mimic the *in vivo* setting we assumed that the stress-free configuration was unavailable. The diastolic configuration $\mathscr{C}_1$ (at 80 mmHg pressure) was chosen as the reference, and deformation tensors relative to this configuration were computed. The finite element parametric coordinates are used as the convected surface coordinates. From the finite element geometry, the convected basis vectors in each deformed configurations are determined according to

$$ {}^{(i)}\mathbf{g}_\alpha = \sum_{I=1}^{Nel} \frac{\partial \Psi_I}{\partial \xi^\alpha} \, {}^{(i)}\mathbf{x}^I, \quad 1 \le i \le N, \tag{21} $$

with the understanding that $\mathbf{G}_\alpha = {}^{(1)}\mathbf{g}_\alpha$. Here N is the number of loaded configuration, Ψ_I are element interpolation functions, and Nel is the total number of nodes per element. The left superscript indicates the load state. Components of the Cauchy-Green deformation tensor are computed by

$$ {}^{(i)}g_{\alpha\beta} = \sum_{I=1}^{Nel} \sum_{I=J}^{Nel} \frac{\partial \Psi_I}{\partial \xi^\alpha} \frac{\partial \Psi_J}{\partial \xi^\beta} \, {}^{(i)}\mathbf{x}^I \cdot {}^{(i)}\mathbf{x}^J, \tag{22} $$

and thus

$$^{(i)}\mathbf{C} = {}^{(i)}g_{\alpha\beta}\mathbf{G}^{\alpha} \otimes \mathbf{G}^{\beta}, \quad 1 < i \leq N. \tag{23}$$

Tensors $^{(i)}\mathbf{C}$ describe strains relative to $\mathscr{C}_1$. At every point in $\mathscr{C}_1$, there is a reference tensor $\mathfrak{G}$ representing the pre-strain from the stress-free configuration to $\mathscr{C}_1$. Strain invariants should be computed according to (10), (12), and (13).

3.4 Inverse stress analysis

The stress distribution in each deformed state was computed individually using the inverse method described in [13]. Note that this analysis needs neither the stress-free configuration nor the material model in question. An auxiliary neo-Hookean model is employed to compute the stress, the strain energy function of which takes the form

$$w = \frac{\nu_1}{2}\left(I_1 - 2\log J - 2\right) + \frac{\nu_2}{4}\left(I_1 - 2\right)^2. \tag{24}$$

Similar to the elastic parameters E_i, the parameters ν_1 and ν_2 here are also effective elastic parameters which are multiplications of 3D elasticity constants with the wall thickness. Parametric values $\nu_1 = \nu_2 = 5.0$ N/mm were used.

In the inverse stress analysis, clamped boundary conditions were applied on the sac boundary in each deformed state. This constraint again is not realistic, but was employed to facilitate the stress computation because it is difficult to define the realistic boundary condition. Due to the presence of displacement constraints, the stress solution is expected to be influenced by the auxiliary material model. But owing to the static determinacy of the system, the influence is expected to occur only in a boundary layer, outside which the solution should approach the static asymptote. In this study, the boundary layer was identified by examining the sensitivity of the inverse stress solution to the material parameters of the auxiliary model. Stress distributions were computed with ν_1 and ν_2 increased by a hundred

times, and compared with the original ones.

3.5 Stress function

Let $\boldsymbol{\sigma}$ be the Cauchy stress in the membrane. As a thin membrane is in general in the plane stress condition, the Cauchy stress has only in-plane components and hence we can write it in the convected system as $\boldsymbol{\sigma} = \sigma^{\alpha\beta}\mathbf{g}_\alpha \otimes \mathbf{g}_\beta$. Assuming the Cauchy stress is uniform over the thickness, a straightforward computation shows that the stress power in an infinitesimal element is $\frac{1}{2}\sigma^{\alpha\beta}\dot{g}_{\alpha\beta}\, hda$ [45, 46]; here h is the current thickness and da is the surface area of the infinitesimal element. By definition of elasticity, we have $\frac{1}{2}\sigma^{\alpha\beta}\dot{g}_{\alpha\beta}\, hda = \dot{w}\, dA$ where dA is the undistorted surface area. Introduce the tension tensor $\mathbf{t} = h\boldsymbol{\sigma}$, noticing $da/dA = J = \sqrt{I_2}$ and $\dot{w} = \frac{\partial w}{\partial g_{\alpha\beta}} \cdot \dot{g}_{\alpha\beta}$, the equality above implies $Jt^{\alpha\beta} = 2\frac{\partial w}{\partial g_{\alpha\beta}}$, and hence

$$t^{\alpha\beta} = \frac{2}{J}\frac{\partial w}{\partial g_{\alpha\beta}}. \tag{25}$$

The tension $\mathbf{t}$ is the stress resultant over the current thickness; for convenience it is still referred to as the stress hereafter.

Recall that we have chosen the diastolic configuration as the reference. Let $\mathbf{N}_I$ be the tangent vector of the I-th fiber at a point in this configuration. Relative to the convected basis we write

$$\mathbf{N}_I = N_I^\alpha \mathbf{G}_\alpha. \tag{26}$$

Under a regular deformation, the tangent vector transforms to $\mathbf{n}_I = \mathbf{F}\mathbf{N}_I$ in the current configuration. Note that neither $\mathbf{N}_I$ nor $\mathbf{n}_I$ is necessarily a unit vector. Noticing $\mathbf{F}\mathbf{G}_\alpha = \mathbf{g}_\alpha$, we find

$$\mathbf{n}_I = N_I^\alpha \mathbf{g}_\alpha. \tag{27}$$

That is, the components of the vector remain invariant in the convected system. Therefore, if the components are specified in one configuration, they are known in all

configurations. In particular, in the (local) natural configuration the fiber tangent must have the form

$$\boldsymbol{\mathcal{N}}_I = N_I^\alpha \boldsymbol{\mathcal{G}}_\alpha. \tag{28}$$

In terms of reference quantities, the fiber stretch is given by

$$\lambda_I^2 = \frac{N_I^\alpha g_{\alpha\beta} N_I^\beta}{N_I^\delta \mathfrak{G}_{\delta\gamma} N_I^\gamma}. \tag{29}$$

Invoking the stress formula (25), specializing it to the energy function (14), noticing $\frac{\partial \lambda_I^2}{\partial g_{\alpha\beta}} = (N_I^\delta \mathfrak{G}_{\delta\gamma} N_I^\gamma)^{-1} N_I^\alpha N_I^\beta$ and $J = \sqrt{\frac{\det[g_{\alpha\beta}]}{\det[\mathfrak{G}_{\delta\gamma}]}}$, we find

$$t^{\alpha\beta} = \sum_{I=1}^{8} \frac{k_I}{2} \sqrt{\frac{\det[\mathfrak{G}_{\alpha\beta}]}{\det[g_{\delta\gamma}]}} \exp\left[a(\lambda_I^2 - 1)^2\right] (\lambda_I^2 - 1) \left(N_I^\delta \mathfrak{G}_{\delta\gamma} N_I^\gamma\right)^{-1} N_I^\alpha N_I^\beta. \tag{30}$$

Since the stretch (29) is invariant under the scaling transformation $\mathbf{N} \mapsto a\mathbf{N}$ for any nonzero a, the fiber tangent can be characterized by one parameter. We can introduce

$$\cos\theta_I = \frac{N_I^1}{\sqrt{(N_I^1)^2 + (N_I^2)^2}}. \tag{31}$$

Note that if in a configuration $\mathbf{g}_1$ and $\mathbf{g}_2$ are orthonormal at a point, then θ is indeed the angle that the fiber I makes with respect to $\mathbf{g}_1$ at that point. In this work, the basis vectors $\{\boldsymbol{\mathcal{G}}_1, \boldsymbol{\mathcal{G}}_2\}$ in the imaged configuration are constructed to be orthonormal everywhere. Thus, θ_I are the fiber angles in this configuration. If we set $\theta_1 = \theta$, angles of other fibers follow as $\theta_I = \theta + \frac{I-1}{8}\pi,\ I = 1, 2, \cdots, 8$, see Figure 1. In this way, the fiber angles are completely parameterized by the parameter θ. Altogether, the Cauchy stress is a function of $g_{\alpha\beta}$, $\mathfrak{G}_{\alpha\beta}$, the material parameters (E_1, E_2, a), and the angle θ.

3.6 Parameter identification

At this point we obtained, at each Gauss point, the Cauchy stress $t^{\alpha\beta}$ and the relative deformation tensor $g_{\alpha\beta}$ for each of the pressurized states. The next step was to fit

the pointwise data to the stress function (30). We denote the stress in the i-th configuration by

$$ {}^{(i)}t^{\alpha\beta} = t^{\alpha\beta}(E_1, E_2, a, \theta, {}^{(i)}g_{\delta\gamma}, \mathfrak{G}_{\delta\gamma}). \tag{32} $$

Let ${}^{(i)}\hat{t}^{\alpha\beta}$ be the "experimental" stress computed from the inverse analysis. The objective function is defined pointwisely, as

$$ \Phi = \sum_{i=1}^{N} \left({}^{(i)}t^{\alpha\beta} - {}^{(i)}\hat{t}^{\alpha\beta} \right) {}^{(i)}g_{\alpha\gamma} \, {}^{(i)}g_{\beta\delta} \left({}^{(i)}t^{\delta\gamma} - {}^{(i)}\hat{t}^{\delta\gamma} \right), \tag{33} $$

where N is the total number of loaded configurations. In tensor notation, $\Phi = \sum_{i=1}^{N} \| {}^{(i)}\mathbf{t} - {}^{(i)}\hat{\mathbf{t}} \|^2$.

The regression problem is formulated as

$$ \begin{array}{ll} \text{minimize} & \Phi\left(E_1, E_2, a, \theta, \mathfrak{G}_{11}, \mathfrak{G}_{22}, \mathfrak{G}_{12}\right) \\ \text{subject to} & \mathfrak{G}_{11} > 0, \quad \mathfrak{G}_{22} > 0, \quad \mathfrak{G}_{11}\mathfrak{G}_{22} - \mathfrak{G}_{12}^2 > 0, \\ & \mathbf{l} \leq [E_1, E_2, a, \theta, \mathfrak{G}_{11}, \mathfrak{G}_{22}, \mathfrak{G}_{12}] \leq \mathbf{u}, \\ & E_1 \geq E_2. \end{array} \tag{34} $$

Here, $\mathbf{l}$ and $\mathbf{u}$ are the lower and upper bounds of the vector of regression variables $[E_1, E_2, a, \theta, \mathfrak{G}_{11}, \mathfrak{G}_{22}, \mathfrak{G}_{12}]$. For both cases, $\mathbf{l} = [0.0, 0.0, 15.0, -\pi, 0.9, 0.9, -0.05]$ and $\mathbf{u} = [1.5, 1.4, 25.0, \pi, 1.05, 1.05, 0.05]$. The constraint, $E_1 \geq E_2$, ensures that the angle between the first principal material axis and the local base vector $\boldsymbol{\mathcal{G}}_1$ be identified, assuming the fibers in the first principal material axis is stiffer than those in the second one. The nonlinear regression was conducted by a gradient-based, sequential quadratic programming (SQP) algorithm, SNOPT [47].

4 Results

4.1 In vivo relative deformation

Figure 4 shows the distribution of the maximum relative principal stretch ratio, λ_1, from the diastolic (80 mmHg) to the systolic (160 mmHg) state for the two cases. For both cases, λ_1 ranged from 1.006 to 1.024. Case II, however, underwent smaller deformation in the dome region than Case I due to relatively stiffer material property. In general, in the regions where the surface curvature was relatively smaller, or in other words flatter, the aneurysm wall was more prone to deformation; therefore higher stretch ratio, $\lambda_1 \approx 1.024$, was reached for Case I, and $\lambda_1 \approx 1.023$ took place for Case II. These regions are represented by the red zones in the contour plots. On the contrary, the regions with initial larger surface curvature underwent less deformation. This phenomenon was especially prominent near the sac tip; e.g., $\lambda_1 \leq 1.018$ occurs for Case I whereas $\lambda_1 \leq 1.012$ took place for Case II. Again, Case II had smaller deformation than Case I. In the most part of the aneurysm sack, i.e., the belly region, medium deformation took place, with $\lambda_1 \approx 1.02$.

4.2 Stress distribution, static determinacy, and boundary layer

We demonstrate the static determinacy of membrane wall stress using Case I. Case II had similar results, so they are not presented here. In a numerical study, the static determinacy of this system can be examined by comparing the stress solutions from the forward analysis (by the reference Kroon-Holzapfel model) and those from the inverse analysis (by the auxiliary neo-Hookean model). In real applications, the "exact stress" is not available and for this reason, we assessed the static determinacy indirectly by examining the stress sensitivity to the auxiliary model. The material

parameters ν_1 and ν_2 were both increased to a hundred times, i.e., $\nu_1 = \nu_2 = 500$ N/mm. The absolute percentage differences of the first principal stress relative to that of the baseline model in three loaded configurations (p=80, 120, and 160 mmHg, respectively) are shown in Figure 5. Overall, the difference was very small, less than 0.05% in most part of the sac. Near the boundary, however, the difference was elevated, especially at higher pressure (see Figure 5(c)). There was approximately five-fold reduction in the stress difference over the four layers of elements near the boundary at 160 mmHg. Based on this observation, we submitted that the stress solution four layers of element above the clamped boundary is a good approximation of the "static stress". The four layers of elements were considered as the boundary layer where the inverse stress solution was deemed inaccurate. This region was excluded in parameter identification.

For the interest of demonstrating the static determinacy, the inverse stress solution was also compared with the forward solution in the same three loaded configurations. Figure 6 shows the deformed geometries and the distributions of the first Cauchy principal stress computed from forward FE analyses (first row) and finite element inverse elastostatics method (second row) by the baseline neo-Hookean model. Clearly, the inverse method re-established the wall stress distribution with a good accuracy, although a totally different material model was utilized in the computation. The third row shows the absolute percentage difference of the first principal stress between the inverse and forward solutions. As can be seen from the contour plots, the differences were less than 1% in the most part of the sac. However, within four layers of elements near the clamped boundary, the difference was relatively more substantial; it ranged from 1% to 5%. Over four layers of elements above the boundary, the difference decreased to under 1%, indicating that the inverse solution approached the static asymptote.

4.3 Parameter identification

Parameter identification was conducted at all Gauss points in the identification zone (the cap region excluding the boundary layer). After the parameters were identified at all Gauss points, they were projected to the nodes by a least-square algorithm.

Figure 7 (a), (b), and (c) show respectively the distribution of the identified elastic parameters E_1, E_2, and a for Case I. Qualitatively judged from the distribution contour, the linear dependence of the identified E_1 and E_2 over the height was recovered. The homogeneous distribution of a was also identified successfully in the most part of the identification zone. The deviations from the reference value were computed at each node. Take E_i for example, the deviation was quantified by the relative error $Error(E_i) = \left|\left(E_i - \tilde{E}_i\right)/\tilde{E}_i\right| \times 100\%$, $(i = 1, 2)$, where $\tilde{E}_i$ are the reference parameters. Figure 7 (d), (e), and (f) show the distribution of the relative errors of E_1, E_2, and a, respectively, in the identification zone. The errors were less than 2%, 3% and 4% for E_1, E_2 and a, respectively, in the most part of the cap. Relatively higher identification error in a ($\geq 10\%$) were found to occur at the regions where the *in vivo* deformation was relatively smaller, e.g., near the sac tip. The scatter dot plots of the distribution of identification error, Figure 7 (g), (h), and (i), clearly show that very small error occurred in a large portion of the identification region, and relatively larger error occurred only at some scattered points. The mean, standard deviation, minimum and maximum of the identification error over the identification zone are listed in Table 1. The mean error for the three parameters was 1.47%, 1.97%, and 2.73%, respectively.

Figure 8 demonstrates the comparison between the identified (red solid line) and true (blue dashed line) first principal direction, which corresponds to the direction of the first collagen fiber, at Gauss points. Overall, the fiber directions were accurately identified in most part of the sac, except for some scattered points.

Table 1: Mean, standard deviation, minimum and maximum of the identification error of the elastic parameters, the stress-free metric tensor components and norm in the cap region of the aneurysm sac for Case I.

	Error(E_1)	Error(E_2)	Error(a)	Error($\mathfrak{G}_{11}$)	Error($\mathfrak{G}_{22}$)	Error($\mathfrak{G}$)
Mean (%)	1.47	1.97	2.73	0.09	0.08	0.14
SD (%)	1.34	1.32	3.33	0.09	0.06	0.07
Min (%)	8.45E-4	7.22E-3	7.08E-3	5.93E-4	8.16E-4	0.02
Max (%)	14.94	7.17	21.67	1.14	0.58	0.87

Similar results were observed for Case II. The identified distribution, distribution of identification error, and scatter dot plot of identification error are shown in Figure 9. The mean, standard deviation, minimum and maximum of the identification error over the identification zone are listed in Table 2. The mean error for the three parameters was 1.18%, 1.79%, and 3.88%, respectively. It is worth noting that the identification of parameter a for Case II was less accurate near the sac tip due to relatively smaller deformation.

Since the stress-free configuration was specified in the forward analysis, the analytical values of $\mathfrak{G}$ can be computed at every Gauss point using Equation (9). The last three columns of Table 1 list the identification errors in $\mathfrak{G}$. The mean errors in the diagonal components were below 0.1% percent. The shear component $\mathfrak{G}_{12}$ was close to zero throughout the domain and therefore could have large but inconsequential error. For this reason the percentage error norm $Error(\mathfrak{G}) = \frac{\|\mathfrak{G}-\mathfrak{G}^{Identified}\|}{\|\mathfrak{G}\|} \times 100\%$ was computed instead. The percentage error norm remained small ($< 0.87\%$) throughout the identification zone, indicating an overall good fit. Similar results for Case II are listed in the last three columns of Table 2.

Table 2: Mean, standard deviation, minimum and maximum of the identification error of the elastic parameters, the stress-free metric tensor components and norm in the cap region of the aneurysm sac for Case II.

	Error(E_1)	Error(E_2)	Error(a)	Error($\mathfrak{G}_{11}$)	Error($\mathfrak{G}_{22}$)	Error($\mathfrak{G}$)
Mean (%)	1.18	1.79	3.88	0.07	0.05	0.09
SD (%)	1.02	1.29	5.06	0.06	0.04	0.04
Min (%)	1.37E-3	1.09E-3	0.02	1.81E-4	6.59E-5	0.01
Max (%)	6.29	9.61	25.0	0.34	0.21	0.29

4.4 Predictability of the identified elastic parameters

We evaluated the predictability of the identified elastic parameters by conducting two forward finite element simulations at an elevated pressure ($p = 170$ mmHg) which was not used in the regression. We only presented the result for Case I since Case II had similar result. As mentioned above, the boundary layer was excluded in the parameter identification process. To facilitate the analysis, the material parameters in the boundary layer were assigned to the reference distribution in both analyses. Figure 10(a) shows the comparison between the predicted deformed configuration from the reference material (solid surface) and that from the identified one (mesh). Evidently, the two deformed configurations matched extremely well. Figure 10(b) shows the node-wise percentage difference, defined as $\|\mathbf{d} - \tilde{\mathbf{d}}\|/\|\tilde{\mathbf{d}}\| \times 100\%$, where $\tilde{\mathbf{d}}$ and $\mathbf{d}$ stand for, respectively, the nodal displacements computed from the reference and the identified materials. The deviation was less than 0.2% in the most part of the aneurysm sac. There were several nodes near the fundus where relatively larger deviation occurred, but the value was still low. The maximum difference was around 1.0%.

5 Discussion

We utilized simulated quasi-static deformations to inversely identify tissue elasticity parameters and the stress-free configuration of a cerebral aneurysm. The numerical model took into account some essential features of CAs, including fully nonlinear anisotropic constitutive behavior, convex but otherwise arbitrary geometry, and spatially varying material properties. The inverse analysis employed only deformations between the diastolic and systolic pressures without the access to the stress-free configuration. The visible strain was below 3%, consistent with the physiological strain range reported in the literature. The study indicated that, even under these conditions, the heterogeneous elasticity parameters and the reference metric can be recovered with reasonable accuracy. The mean errors of stiffness parameters E_1 and E_2 were less than 2% for the two cases of heterogeneity. The exponent a, which is an indicator of nonlinearity, was less accurate, but the mean error was still reasonably small (2.73% for Case I and 3.88% for Case II). The mean errors of the diagonal elements as well as the percentage error norm of $\mathfrak{G}$ were on the order of 0.1%.

Identifying the stress-free geometry is a challenging task in inverse analysis. There seems to have two possible ways; one is to consider the geometry globally, the other locally. The present work follows the second route; the stress-free geometry is parameterized by a reference metric that represents the pre-strain from the local stress-free configuration to the chosen reference configuration. This scheme fits well the point-wise identification framework, as it entails only three additional parameters in the local optimization problem. However, it remains to assess whether the identified reference metric can represent the stress-free configuration in a meaningful way. In this work, we evaluated the metric identification by comparing with their theoretical values point-wisely. In real application, there is no analytical metric to compare with and hence the verification must be conducted alternatively. A possible way is to con-

struct a global stress-free configuration from the identified metric field and verify the geometric result (together with material parameters) through forward analyses. If the identified metric corresponds to a tensor field $\mathfrak{G}$ derived from a global stress-free configuration for which the material point position is $\mathbf{X}_0(P)$, then, in theory

$$\mathfrak{G}_{\alpha\beta} := \frac{\partial \mathbf{X}_0}{\partial \xi^\alpha} \cdot \frac{\partial \mathbf{X}_0}{\partial \xi^\beta} = \mathfrak{G}^{Identified}_{\alpha\beta}. \tag{35}$$

The problem of recovering $\mathbf{X}_0$ can be formulated using the least square method minimizing the functional $J = \int_B \|\mathfrak{G} - \mathfrak{G}^{Identified}\|^2 \, dV$, which gives the weak form

$$\int_B \delta\mathfrak{G} \cdot \left[\mathfrak{G} - \mathfrak{G}^{Identified}\right] dV = 0, \tag{36}$$

subject to the boundary condition that $\mathbf{X}_0 = \mathbf{0}$ along the clamped edge. The computation can be carried out in the finite element framework by introducing a surrogate elasticity model with the stress function $\mathbf{S} = \mu(\mathfrak{G} - \mathfrak{G}^{identified})$, and solving for the nodal values of $\mathbf{X}_0$ in exactly the same manner as solving a finite strain problem with prescribed initial strains. Note that this procedure is in fact a method for constructing a global stress-free configuration from a given metric field. In this study, we did not conduct this computation because we had the luxury of having the analytical metric data. Judged from quality of the metric fit, if we would perform this computation the recovered stress-free configuration is expected to match well the prescribed one.

The identification accuracy correlated closely with the magnitude of *in vivo* deformation, especially for parameter a. As shown by Figure 4 and Figures 7 and 9, the identification error was generally smaller in the region where the *in vivo* deformation was larger. This is expected, because the nonlinear behavior is better exposed at a wider strain range. In order to further elucidate such a phenomenon, we increased the *in vivo* deformation by enlarging the pressure range to 50-200 mmHg for Case I. The distribution of the maximum principal stretch ratio is shown in Figure 11. The

maximum principal stretch ratio near the sac tip increased from 1.018 to 1.03 (the maximum stretch over the entire sac is 1.047). The identification results presented significant improvement. Figure 12 shows the distribution and scatter dot plots of the identification errors. The mean identification errors for the three parameters decreased to 1.13%, 1.82%, and 0.53%, respectively. The identification accuracy of parameter a presented the most substantial improvement since it dictates the shape of the stress-strain curve; therefore, the wider the strain range undergone, the more accurately it can be identified. For example, the identification error decreased from larger than 10% to less than 2%. Regardless of the pressure range, if the visible strain range is further reduced, the quality of the identification result is expected to degrade.

Clamped boundary condition was used in this study. This constraint is not realistic for *in vivo* condition, and induces a boundary effect that needs to be carefully addressed. In the simulation, we identified the boundary layer numerically by comparing the stress variations under the change of material parameters of the auxiliary model. In essence, we are using stress insensitivity to assess static determinacy; the former is a necessary condition for the later. The boundary layer was subsequently excluded in the inverse analysis. As reported above, the identification results outside the boundary layer appear to be accurate. In real applications, it is difficult to define the realistic boundary conditions. The study suggests that, as a practical strategy, clamped boundary condition may be used as long as the boundary effect is properly considered.

There are some limitations in this study. First, although the sac is image-based, the geometry appears to be more regular than that of realistic aneurysms. As the sac is convex, it is described as an elastic membrane. Real aneurysms contain undulated surface features, for which an appropriate description should be a shell structure.

The method of stress analysis hinges critically on the property static determinacy, which would be compromised if significant bending and transverse shear are necessary for equilibrium. Nevertheless, our pervious study indicated that, even for shell structure having concave surface features, there exist regions where the membrane response dominates and in such regions, the in-plane stress appears to remain statically determined [25]. We submit that the proposed method can also be applied to some shell structures, at lease regionally. Second, we did not investigate the effect of numerical noise. Adding noises to the displacement data can help to understand the robustness of the method. These limitations will be addressed in a future study.

The proposed method is not directly applicable to clinical study yet. A major stumbling block, as alluded in the introduction, is the limitation of image resolution. In a carefully designed study, Balocco et al. [16] examined the feasibility of cerebral aneurysm *in vivo* identification using simulated image data. They incorporated realistic geometries but linear elastic constitutive equations with regional properties. They found that the minimum spatial resolution necessary for inversely resolving the material elasticity is 0.1mm, and therefore concluded that image-based identification at the current resolution is infeasible. However, they used a traditional optimization approach that optimizes the parameters altogether by minimizing the difference of nodal displacements. It is known that elasticity parameters have a global influence on displacement in elasticity problems, and thus, displacement-based optimization cannot sharply characterize heterogeneous distributions. In this regard, there is a room to improve their inverse analysis, and possibly lower the resolution requirement although the outcome is unlikely to change the conclusion. In the present study, the displacement in high strain regions was on the order of hundreds of microns. Suppose ten loaded configurations are to be obtained for parameter identification, the required resolution should be around tens of microns. The current diagnostic imag-

ing is unlikely to meet this requirement. Also, the present study did not consider numerical noises, the presence of which is expected to further raise the resolution requirement. Nevertheless, the value of this study lies in that it clearly demonstrated the potential of the proposed method, setting aside image issues.

Imaging technologies and registration methods are rapidly advancing. Hayakawa et al. [48] utilized electrocardiographic (ECG)-gated multislice CT angiography imaged aneurysm wall motion in four dimensions by adding the dimension of time to 3D images. Yaghmai et al. [49] reported four-dimensional (4D) imaging of aneurysm phantom pulsatility with the dynamic multiscan method and showed improvement in image quality compared with ECG-gated imaging. These studies showed the dynamic imaging can capture the local pulsation of CAs. Recent studies by Zhang et al. [50, 51] *quantified* the dynamic motion by recovering dynamic 3D vascular morphology from a single 3D rotational X-ray angiography acquisition. The dynamic morphology corresponding to a canonical cardiac cycle was represented via a 4D B-spline based spatiotemporal deformation, which was estimated by simultaneously matching the forward projections of a sequence of the temporally deformed 3D reference volume to the entire 2D measured projection sequence. The technique was validated using digital and physical phantoms of pulsating cerebral aneurysms. The registration error was reported to within 10% of the pulsation range. Oubel et al. [52] reported a method of 2D wall motion estimation which combines non-rigid registration with signal processing techniques to measure pulsation in patients from high frame rate digital subtraction angiography. They have obtained waveforms with magnitude in the range of 0-0.3 mm. Recently, high resolution (0.035 mm) imaging modalities such as Region of Interest rotational micro-angio fluoroscopy [53] and microscope-integrated fluorescence angiography [54] offer promise of significantly richer wall motion data that this method could leverage. Hopefully, the advance of

imaging technologies and registration methods will eventually reach a resolution sufficient for the proposed application.

In summary, this article proposed a method for characterizing aneurysm tissues at the presence of unknown stress-free configuration and tested the feasibility numerically. The uniqueness of the method is the simultaneous identification of nonlinear parameters, collagen fiber orientation, and the reference metric using pointwise stress-strain data. Although not directly applicable to clinical studies yet, the work addressed an important issue facing the future development of *in vivo* identification technology. Future studies include investigating the influence of concave surface features, examining the robustness of the method at the presence of numerical noise, and eventually incorporating real image data. Research along this direction is underway in the authors' group.

Acknowledgements

The work was funded by the National Science Foundation grant CMS 03-48194 and the NIH(NHLBI) grant 1R01HL083475-01A2. These supports are gratefully acknowledged.

References

[1] A. Ronkainen and J. Hernesniemi. Subarachnoid haemorrhage of unknown aetiology. *Acta Neurochirurgica*, 119(1):29–34, 1992.

[2] M. R. Crompton. Mechanism of growth and rupture in cerebral berry aneurysms. *British Medical Journal*, 1:1138–1142, 1966.

[3] N. F. Kassel and J. C. Torner. Size of intracranial aneurysms. *Neurosurgery*, 12:291–297, 1983.

[4] H. Ujiie, K. Sato, H. Onda, A. Oikkawa, M. Kagawa, K. Atakakura, and N. Kobayashi. Clinical analysis of incidentally discovered unruptured aneurysms. *Stroke*, 24:1850–1856, 1993.

[5] D. O. Wiebers, J. P. Whisnant, T. M. Sundt, and W. M. O'Fallon. The significance of unruptured intracranial saccular aneurysms. *Journal of Neurosurgery*, 66:23–29, 1987.

[6] D. O. Wiebers et al. Unruptured intracranial aneurysms risk of rupture and risks of surgical intervention. international study of unruptured intracranial aneurysms investigators. *The New England Journal of Medicine*, 339:1725–1733, 1998.

[7] H. Ujiie, H. Tachibana, O. Hiramatsu, A. L. Hazel, T. Matsumoto, and Y. Ogasawara et al. Effects of size and shape (aspect ratio) on the hemodynamics of saccular aneurysms: a possible index for surgical treatment of intracranial aneurysms. *Neurosurgery*, 45:119–130, 1998.

[8] H. Ujiie, Y. Tamano, K. Sasaki, and T. Hori. Is the aspect ratio a reliable index for predicting the rupture of a saccular aneurysm? *Neurosurgery*, 48:495–503, 2001.

[9] M. L. Raghavan, B. Ma, and R. E. Harbaugh. Quantified aneurysm shape and rupture risk. *Journal of Neurosurgery*, 102:355–362, 2005.

[10] S. K. Kyriacou and J. D. Humphrey. Influence of size, shape and properties on the mechanics of axisymmetric saccular aneurysms. *Journal of Biomechanics*, 29:1015–1022, 1996.

[11] A. D. Shah, J. L. Harris, S. K. Kyriacou, and J. D. Humphrey. Further roles of geometry and properties in the mechanics of saccular aneurysms. *Computational Methods in Biomechanical and Biomedical Engineering*, 1:109–121, 1998.

[12] B. Ma, J. Lu, R. E. Harbaugh, and M. L. Raghavan. Nonlinear anisotropic stress analysis of anatomically realistic cerebral aneurysms. *ASME Journal of Biomedical Engineering*, 129:88–99, 2007.

[13] J. Lu, X. Zhou, and M. L. Raghavan. Inverse method of stress analysis for cerebral aneurysms. *Biomechanics and Modeling in Mechanobiology*, 7:477–486, 2008.

[14] M. Toth, G. L. Nadasy, I. Nyary, T Kernyi, and E. Monos. Are there systemic changes in the arterial biomechanics of intracranial aneurysm patients? *European Journal of Physiology*, 439:573–578, 2000.

[15] T. Anderson. Arterial stiffness or endothelial dysfunction as a surrogate marker of vascular risk. *Candaian Journal of Cardiology*, 22:72B–80B, 2006.

[16] S. Balocco, O. Camara, E. Vivas, T. Sola, L. Guimaraens, H. A. F. Gratama van Andel, C. B. Majoie, J. M. Pozoc, B. H. Bijnens, and A. F. Frangi. Feasibility of estimating regional mechanical properties of cerebral aneurysms in vivo. *Medical Physics*, 37:1689–1706, 2010.

[17] J. Lu and X. Zhao. Pointwise identification of elastic properties in nonlinear hyperelastic membranes. Part I: Theoretical and computational developments. *ASME Journal of Applied Mechanics*, 76:061013/1–061013/10, 2009.

[18] X. Zhao, X. Chen, and J. Lu. Pointwise identification of elastic properties in nonlinear hyperelastic membranes. Part II: Experimental validation. *ASME Journal of Applied Mechanics*, 76:061014/1–061014/8, 2009.

[19] S. Govindjee and P. A. Mihalic. Computational methods for inverse finite elastostatics. *Computer Methods in Applied Mechanics and Engineering*, 136:47–57, 1996.

[20] S. Govindjee and P. A. Mihalic. Computational methods for inverse deformations in quasi-incompressible finite elasticity. *International Journal for Numerical Methods in Engineering*, 43:821–838, 1998.

[21] J. Lu, X. Zhou, and M. L. Raghavan. Inverse elastostatic stress analysis in pre-deformed biological structures: Demonstration using abdominal aortic aneurysm. *Journal of Biomechanics*, 40:693–696, 2007.

[22] X. Zhou and J. Lu. Inverse formulation for geometrically exact stress resultant shells. *International Journal for Numerical Methods in Engineering*, 74:1278–1302, 2008.

[23] X. Zhao, M. L. Raghavan, and J. Lu. Identifying heterogeneous anisotropic properties in cerebral aneurysms: a pointwise approach. *Biomechanics and Modeling in Mechanobiology*, in press, DOI 10.1007/s10237-010-0225-7.

[24] X. Zhou and J. Lu. Estimation of vascular open configuration using finite element inverse elastostatic method. *Engineering with Computers*, 25:49–59, 2009.

[25] Xianlian Zhou, Madhavan Raghavan, Robert Harbaugh, and Jia Lu. Patient-Specific wall stress analysis in cerebral aneurysms using inverse shell model. *Annals of Biomedical Engineering*, 38(2):478–489, 2010.

[26] M .W. Gee, C. Reeps, H. H. Eckstein, and W. A. Wall. Prestressing in finite deformation abdominal aortic aneurysm simulation. *Journal of Biomechanics*, 42:1732–1739, 2009.

[27] M. W. Gee, Ch. Forster, and W. A. Wall. A computational strategy for prestressing patient-specific biomechanical problems under finite deformation. *International Journal for Numerical Methods in Biomedical Engineering*, 26:52–72, 2010.

[28] Jia Lu. A covariant constitutive theory for anisotropic hyperelastic solids with initial strains. *Mathematics and Mechanics of Solids*, in press, http://css.engineering.uiowa.edu/˜jialu.

[29] W. Noll. A mathematical theory of the mechanical behavior of continuous media. *Archive for Rational Mechanics and Analysis*, 2:197–226, 1958/59.

[30] E. H. Lee. Elastic-plastic deformation at finite strains. *ASME Journal of Applied Mechanics*, 36:1–6, 1969.

[31] G.A. Maugin and M. Epstein. Geometrical material structure of elastoplasticity. *International Journal of Plasticity*, 14:109–115, 1998.

[32] E. K. Rodriguez, A. Hoger, and A. D. Mcculloch. Stress-dependent finite growth in soft elastic tissues. *Journal of Biomechanics*, 27:455–467, 1994.

[33] L. A. Taber. Biomechanics of growth, remodeling, and morphogenesis. *Applied Mechanics Review*, 48:487–545, 1995.

[34] E. R. Jacobs and A. Hoger. The use of a virtual configuration in formulating constitutive equations for residually stressed elastic materials. *Journal of Elasticity*, 41:177–215, 1995.

[35] A. Hoger. Virtual configurations and constitutive equations for residually stressed bodies with material symmetry. *Journal of Elasticity*, 48:125–144, 1997.

[36] J. Stålhand, A. Klarbring, and M. Karlsson. Towards in vivo aorta material identification and stress estimation. *Biomechanics and Modeling in Mechanobiology*, 2:169–186, 2004.

[37] T. Olsson, J. Stålhand, and A. Klarbring. Modeling initial strain distribution in soft tissues with application to arteries. *Biomechanics and Modeling in Mechanobiology*, 5:27–38, 2006.

[38] J. Stålhand. Determination of human arterial wall parameters from clinical data. *Biomechanics and Modeling in Mechanobiology*, 8:141–148, 2009.

[39] M. Kroon and G. A. Holzapfel. A new constitutive model for multi-layered collagenous tissues. *Journal of Biomechanics*, 41:2766–2771, 2008.

[40] M. Kroon and G. A. Holzapfel. Estimation of the distribution of anisotropic, elastic properties and wall stresses of saccular cerebral aneurysms by inverse analysis. *Proceedings of the Royal Society of London, Series A*, 464:807–825, 2008.

[41] P. B. Canham, H. M. Finlay, and S. Y. Tong. Stereological analysis of the layered collagen of human intracranial aneurysms. *Journal of Microscopy*, 183:170–180, 1996.

[42] J. Frosen, A. Piippo, A. Paetau, M. Kangasniemi, M. Niemela, J. Hernesniemi, and J. Jaaskelainen. Remodeling of saccular cerebral artery aneurysm wall is associated with rupture: Histological analysis of 24 unruptured and 42 ruptured cases. *Stroke*, 35(10):2287–2293, 2004.

[43] K. Kataoka, M. Taneda, T. Asai, A. Kinoshita, M. Ito, and R. Kuroda. Structural fragility and inflammatory response of ruptured cerebral aneurysms :

A comparative study between ruptured and unruptured cerebral aneurysms. *Stroke*, 30(7):1396–1401, 1999.

[44] R. L. Taylor. FEAP User Manual: v7.5. Technical report, Department of Civil and Environmental Engineering, University of California, Berkeley, 2003.

[45] A. E. Green and J. E. Adkins. *Large Elastic Deformations*. Clarendon Press, Oxford, 2nd edition, 1970.

[46] T. C. Doyle and J. L. Ericksen. Nonlinear elasticity. *Advances in Applied Mechanics*, 4:53–115, 1956.

[47] P. E. Gill, W. Murray, and M. A. Saunders. SNOPT: An SQP algorithm for large-scale constrained optimization. *SIAM Review*, 47:99–131, 2005.

[48] M. Hayakawa, K. Katada, H. Anno, S. Imizu, J. Hayashi, K. Irie, M. Negoro, Y. Kato, T. Kanno, and H. Sano. CT angiography with electrocardiographically gated reconstruction for visualizing pulsation of intracranial aneurysms: Identification of aneurysmal protuberance presumably associated with wall thinning. *American Journal of Neuroradiology*, 26(6):1366–1369, 2005.

[49] V. Yaghmai, M. Rohany, A. Shaibani, M. Huber, H. Soud, E. J. Russell, and M. T. Walker. Pulsatility imaging of saccular aneurysm model by 64-Slice CT with dynamic multiscan technique. *Journal of Vascular and Interventional Radiology*, 18(6):785–788, 2007.

[50] C. Zhang, M. Craene, M. Villa-Uriol, J. M. Pozo, B. H. Bijnens, and A. F. Frangi. Estimating continuous 4D wall motion of cerebral aneurysms from 3D rotational angiography. In *Proceedings of the 12th International Conference on Medical Image Computing and Computer-Assisted Intervention: Part I*, pages 140–147, London, UK, 2009. Springer-Verlag.

[51] C. Zhang, M. C. Villa-Uriol, M. De Craene, J. Pozo, and A. Frangi. Morphodynamic analysis of cerebral aneurysm pulsation from timeresolved rotational angiography. *IEEE Transactions on Medical Imaging*, 28:1105–1116, 2009.

[52] E. Oubel, J. R. Cebral, M. De Craene, R. Blanc, J. Blasco, J. Macho, C. M. Putman, and A. F. Frangi. Wall motion estimation in intracranial aneurysms. *Physiological Measurement*, 31(9):1119–1135, 2010.

[53] V. Patel, K. R. Hoffmann, C. N. Ionita, C. Keleshis, D. R. Bednarek, and R. Rudin. Rotational micro-CT using a clinical C-arm angiography gantry. *Medical Physics*, 35:4757–4764, 2008.

[54] A. Raabe, J. Beck, R. Gerlach, M. Zimmermann, and V. Seifert. Near-infrared indocyanine green video angiography: a new method for intraoperative assessment of vascular flow. *Neurosurgery*, 52:132–139, 2003.

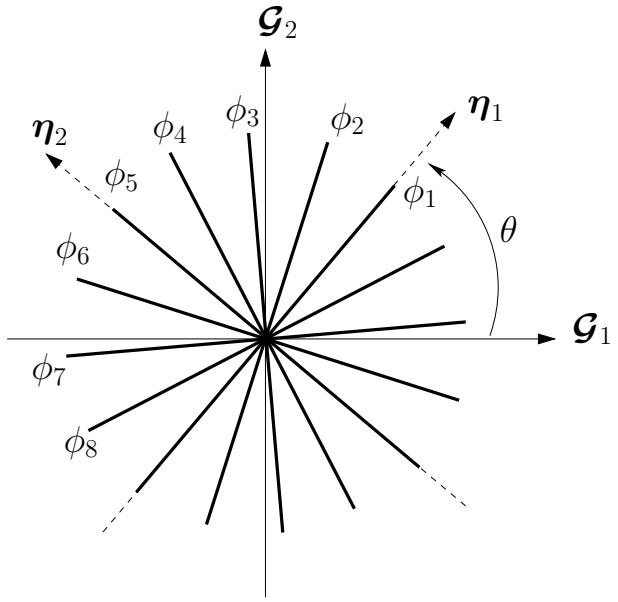

Figure 1: Schematic representation of local fiber distribution in the stress-free state, with respect to a local basis $\boldsymbol{\mathcal{G}}_1 - \boldsymbol{\mathcal{G}}_2$ (Adapted from [39, 40]).

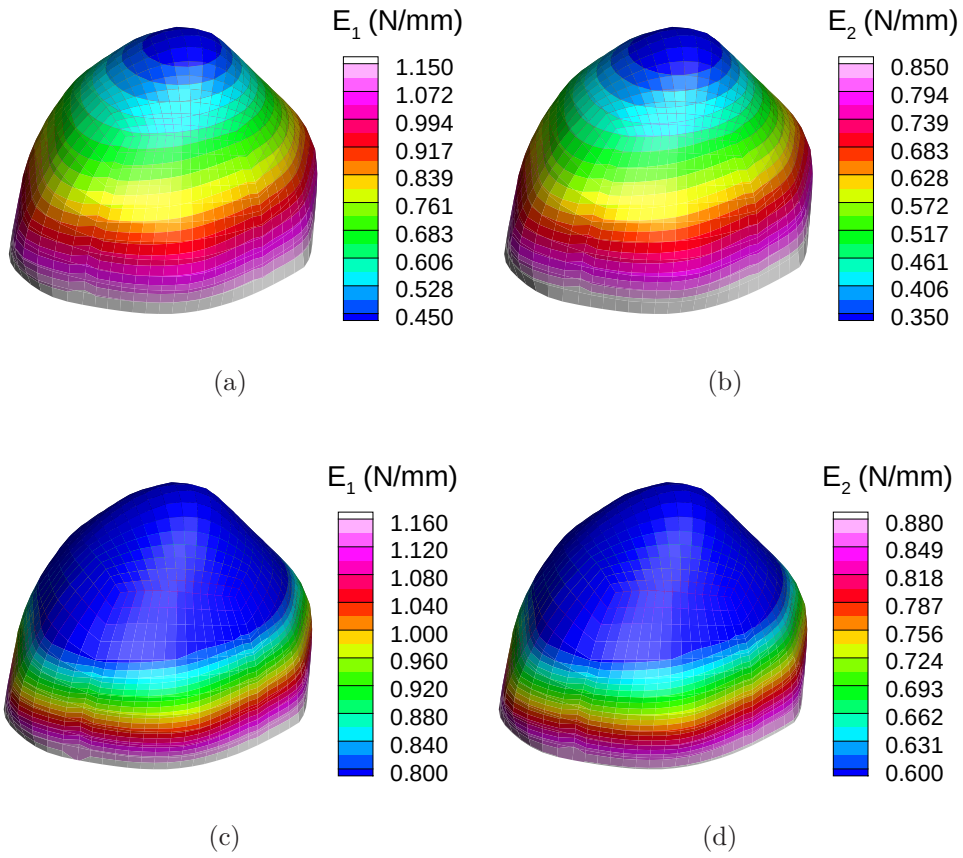

Figure 2: The reference distributions of the elastic parameters E_1 and E_2. Upper row: Case I; Lower row: Case II.

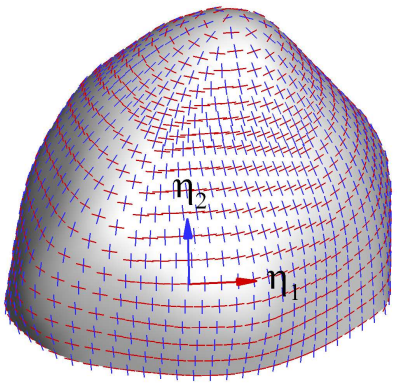

Figure 3: Distribution of the first principal direction $\boldsymbol{\eta}_1$ (red lines) and the second principal direction $\boldsymbol{\eta}_2$ (blue lines), which correspond to the first and fifth collagen fiber directions, respectively.

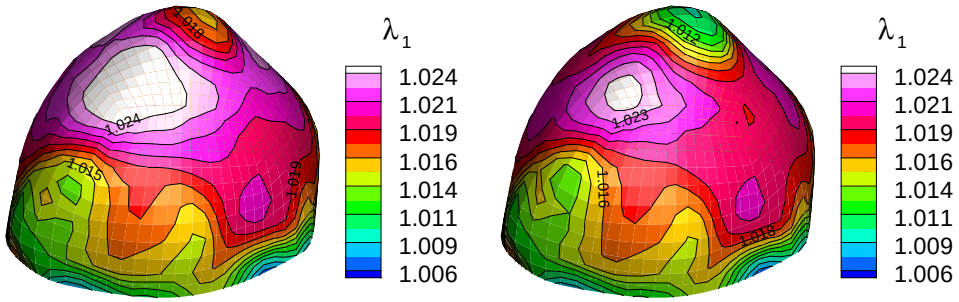

(a) (b)

Figure 4: Distribution of the relative maximum stretch ratio from 80 mmHg to 160 mmHg: (a) Case I; (b) Case II.

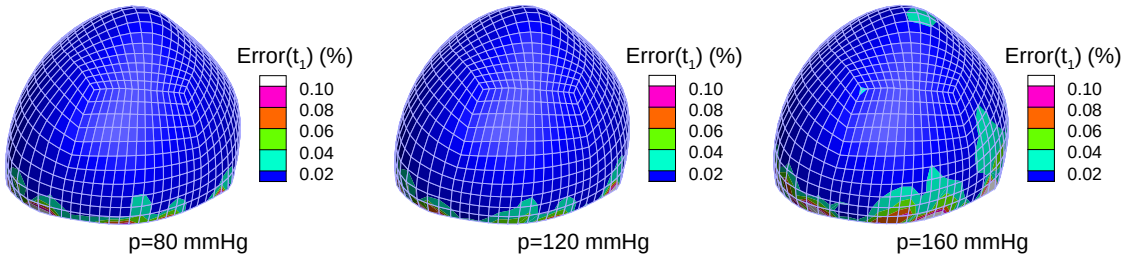

(a) (b) (c)

Figure 5: Absolute relative percentage difference of the first principal stress at variously pressures after increasing the baseline material parameters in the modified neo-Hookean model by 100 times, i.e., $\nu_1 = \nu_2 = 500$ N/mm.

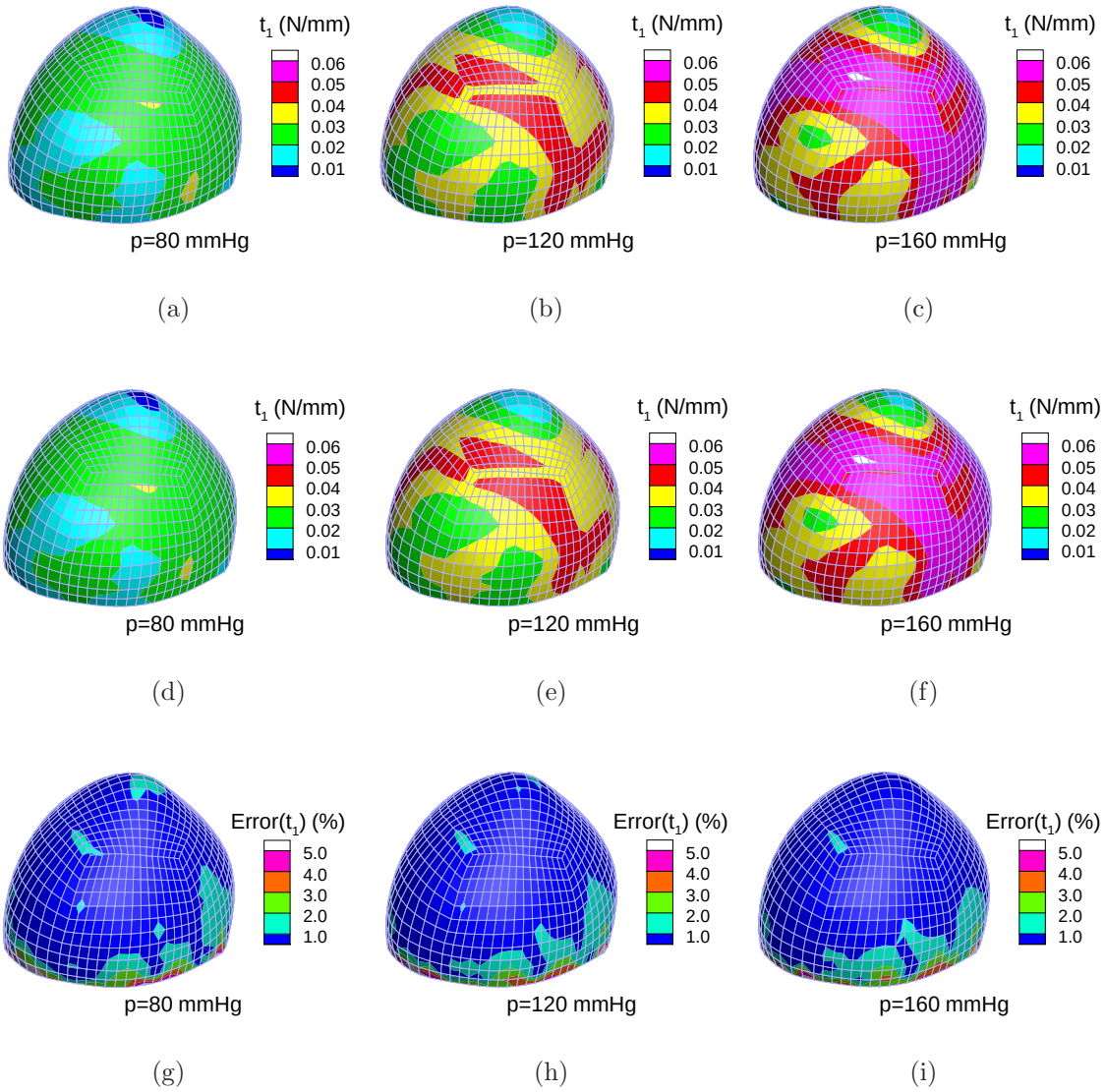

Figure 6: Three of the seventeen loaded configurations and the distribution of the first principal stress computed from forward FE analyses (first row) and finite element inverse elastostatics method (second row). Third row: Absolute relative percentage difference of the first principal stress between the inverse and forward solutions.

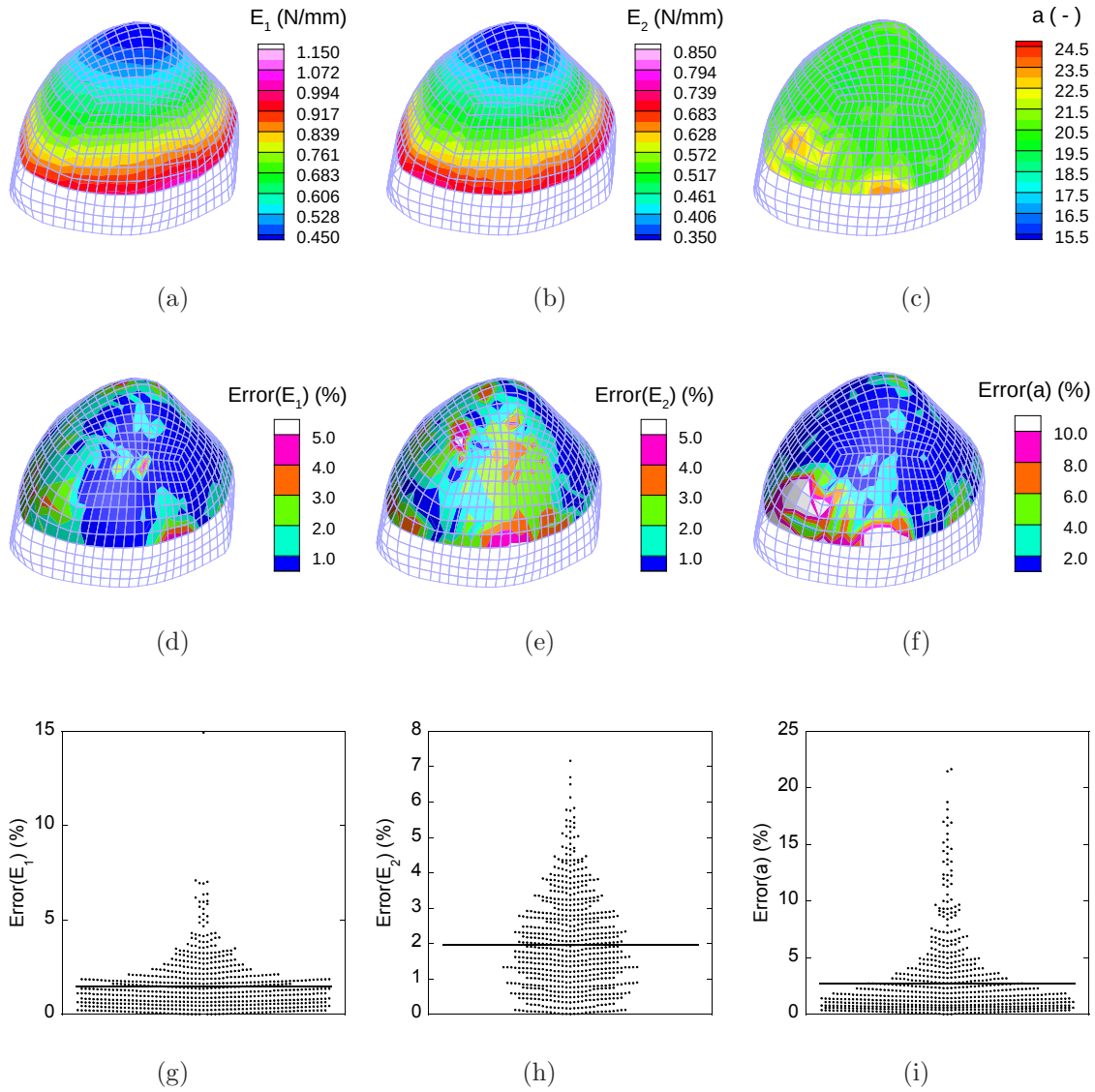

Figure 7: Identification results for Case I. First row: The identified distributions; Second row: Distribution of the identification errors; Third row: Scatter dot plots of the identification errors. The total number of dots at particular y is the occurrence of that value. The horizontal line indicates the mean.

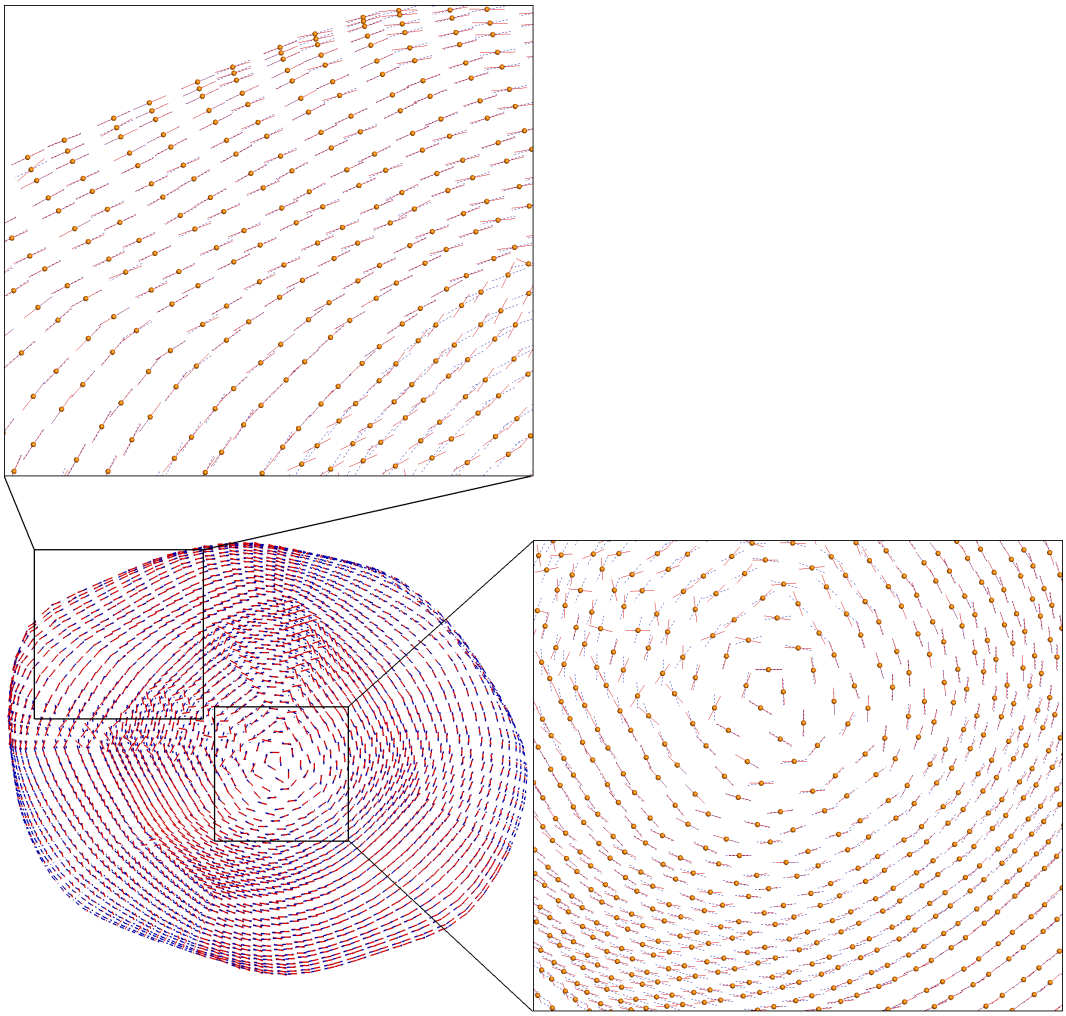

Figure 8: Comparison between the identified (red solid lines) and true (blue dashed lines) first principal direction $\boldsymbol{\eta}_1$, which correspond to the first collagen fiber direction. The fiber directions are plotted at the Gauss points (orange dots).

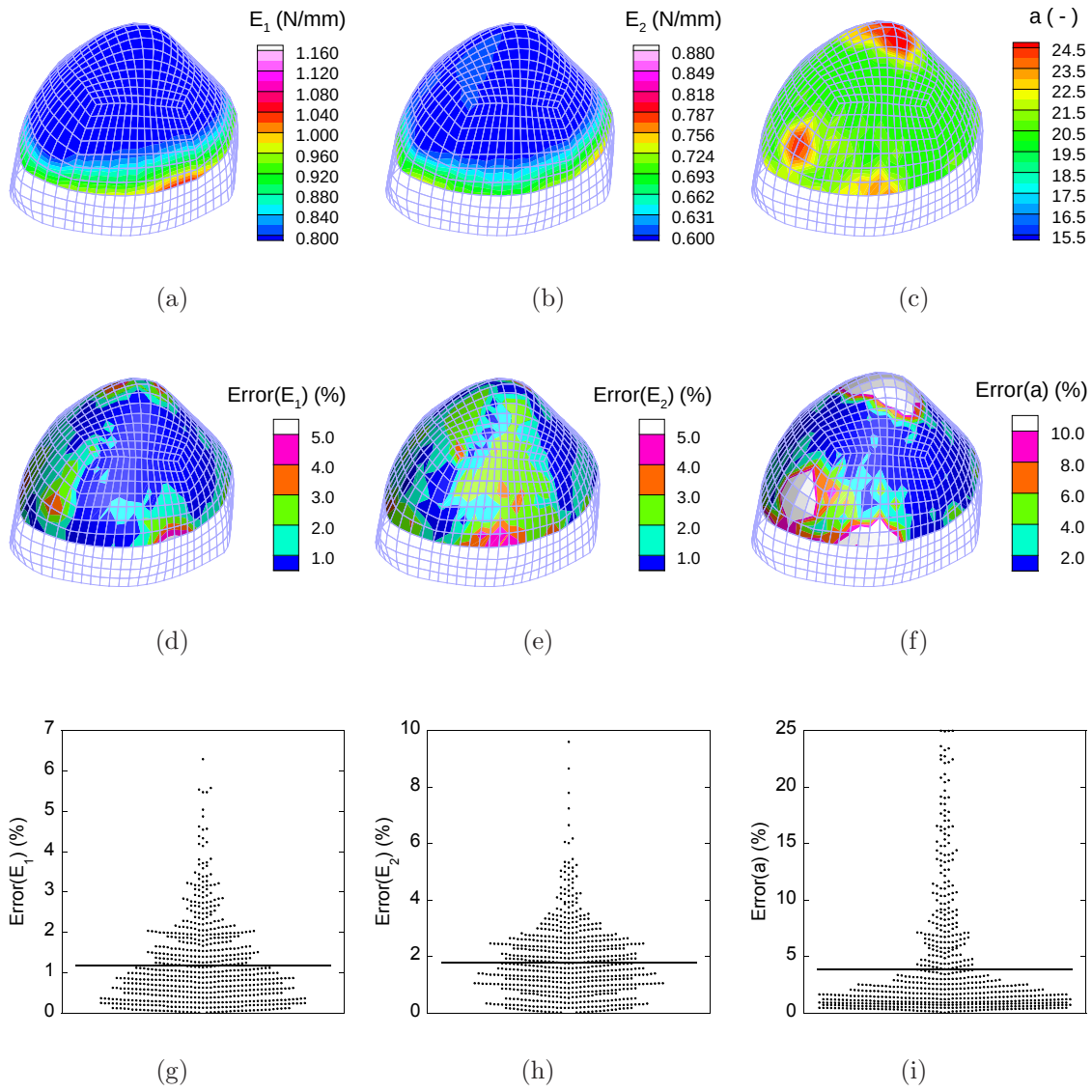

Figure 9: Identification results for Case II. First row: The identified distributions; Second row: Distribution of the identification errors; Third row: Scatter dot plots of the identification errors.

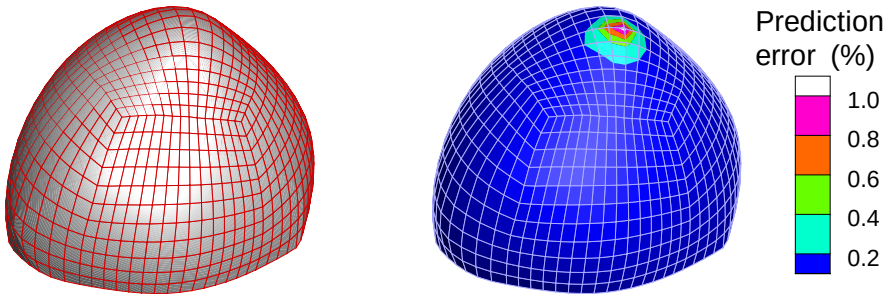

(a) (b)

Figure 10: Predictability of the identified elastic property distribution for Case I: (a) Predicted loaded configurations from the reference material (solid surface) and the identified material (mesh) at 170 mmHg; (b) Percentage deviation in nodal displacement.

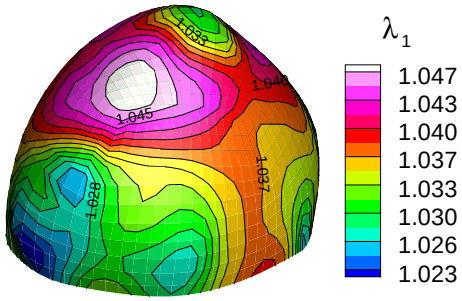

Figure 11: Distribution of the relative maximum stretch ratio from 50 mmHg to 200 mmHg for Case I with a widened pressure range.

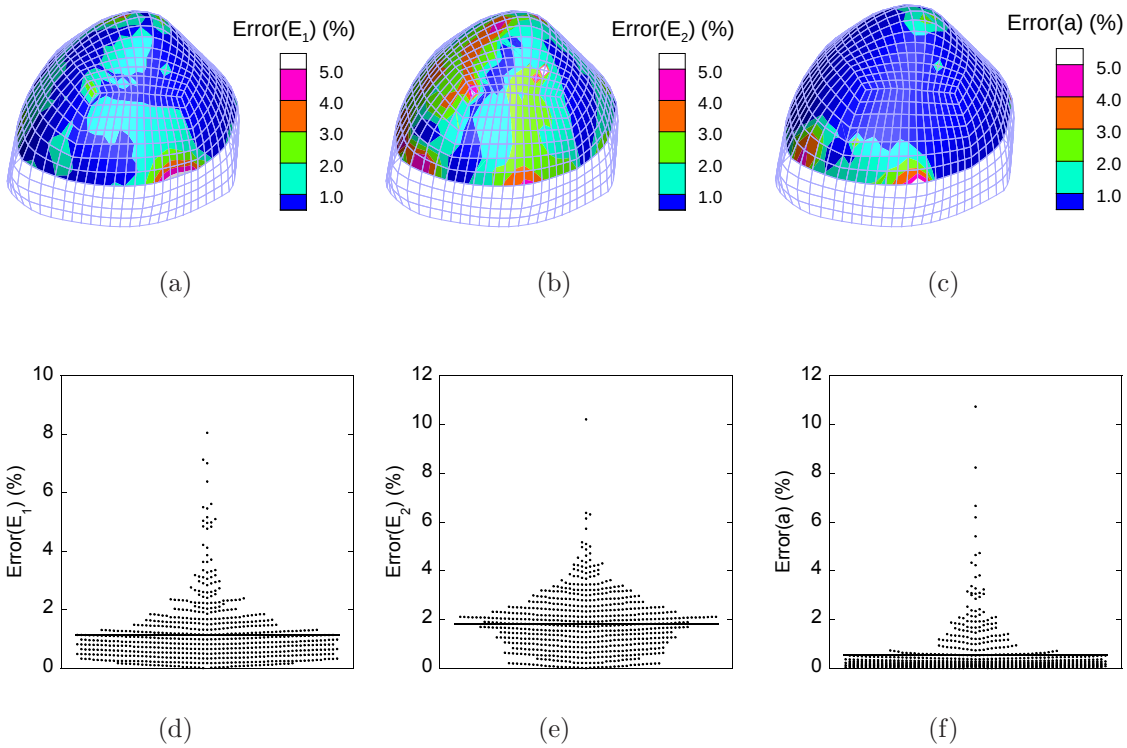

Figure 12: Identification results for Case I with larger *in vivo* deformation. Upper row: Distribution of the identification errors; Lower row: Scatter dot plots of the identification errors.